A Computer Vision Non-Contact 3D System to Improve Fingerprint Acquisition

Georgios Balogiannis[a]*, Dido Yova[b], Konstantinos Politopoulos [c]

[a,b,c] *Laboratory of Biomedical Optics and Applied Biophysics, School of Electrical and Computer Engineering,*
National Technical University of Athens, Iroon Politechniou 9, Zografou Campus, Athens 15780, Greece.
[a]*Email: gmpalog@central.ntua.gr*
[b]*Email: didoy@central.ntua.gr*
[c]*Email: policent@central.ntua.gr*

Abstract

The fingerprint is one of the most important biometrics, with many acquisition methods developed over the years. Traditional 2D acquisition techniques produce nonlinear distortions due to the forced flattening of the finger onto a 2D surface. These random elastic deformations often introduce matching errors, making 2D techniques less reliable. Inevitably non-contact 3D capturing techniques were developed in an effort to deal with these problems. In this study we present a novel non-contact single camera 3D fingerprint reconstruction system based on fringe projection and a new model for approximating the epidermal ridges. The 3D shape of the fingerprint is reconstructed from a single 2D shading image in two steps. First the original image is decomposed into structure and texture components by an advanced Meyer algorithm. The structural component is reconstructed by a classical fringe projection technique. The textural component, containing the fingerprint information, is restored using a specialized photometric algorithm we call Cylindrical Ridge Model (CRM). CRM is a photometric algorithm that takes advantage of the axial symmetry of the ridges in order to integrate the illumination equation. The two results are combined together to form the 3D fingerprint, which is then digitally unfolded onto a 2D plane for compatibility with traditional 2D impressions. This paper describes the prototype 3D imaging system developed along with the calibration procedure, the reconstruction algorithm and the unwrapping process of the resulting 3D fingerprint, necessary for the performance evaluation of the method.

Keywords: Biometrics; fingerprint; 3D reconstruction; non-contact; single-view; fringe projection.

----

* Corresponding author.

1. Introduction

The term biometrics derives from the Greek word "βιομετρία" (viometria), meaning "the measurement of living things". Fingerprint is one of the most important and easy to acquire biometrics and has been widely investigated over the years. 2D ink based techniques came first at the middle of the 19th century. Since then many automated systems have emerged along with the advance of technology. Today fingerprint images are commonly captured with the help of touch based techniques that record high ridge-valley contrast [1]. However, the fingerprint is a 3D feature and when it is forced onto a flat 2D surface during image acquisition it gets distorted, generally in a nonlinear way [2,3,4]. These distortions are irregular and depend on a number of random factors regarding the amount of pressure applied on the finger, the overall shape of the fingertip and possible rolling of the finger. As a result intra-class variations are introduced among fingerprints of the same person, making the 2D contact techniques less reliable and objective.

In order to tackle these problems 3D non-contact imaging techniques began to develop. 3D fingerprint acquisition methods can be considered the future of fingerprint biometrics, as the 3rd dimension provides an additional parameter for biometric coding. Generally, these methods capture the skin surface from a distance, and then use a specific computer vision algorithm to reconstruct the fingerprint. They can be categorized into three main groups: multi-view reconstruction, laser scanning and structured light scanning. Multi-view reconstruction methods can give satisfactory results, but they utilize multiple camera systems, fact that increases the complexity and the cost of the system and can lead to inconsistencies due to false camera calibration and multi-image correspondence errors [5,6]. Laser scanning is more reliable but the 3D data acquisition procedure usually requires a substantial amount of time, which is not very practical for living subjects due to its sensitivity to movement [7,8]. Fringe projection techniques can combine speed with simplicity, making them more suitable for "online" capturing of fingerprints [9]. Despite their indisputable advantages, all fringe projection techniques fall short in the case of highly detailed surfaces as a substantial volume of data gets lost between the projected fringe lines, resulting to low resolving power. Therefore the reconstruction of fingerprints with these methods becomes extremely challenging, since skin comprises both small scale (epidermal ridges) and large scale (overall finger curvature) characteristics [10,11]. The phase-shifting fringe techniques attempt to solve the above problem, but they involve expensive hardware (e.g. DLP projectors) and complicated algorithms [3,12].

In this study we present a simple single-view non-contact imaging system for 3D fingerprint acquisition that involves a fringe pattern projection method. The solution we propose in order to increase the accuracy of the fringe method involves the decomposition of the captured shading image I_f into a structural and a textural component. The structural part u contains the large scale geometrical features of the fingertip (finger curvature) while the textural component v the small scale oscillating variations that correspond to the epidermal ridges. Since the structural part u may contain some unwanted information, like albedo variations of the skin, it is replaced by the geometrical reconstruction provided by the fringe projection process, and the result is a rough approximation of the original surface without the small scale details. The detailed component v is reconstructed by approximating the epidermal ridges with a curved cylindrical structure in a photometric process called Cylindrical Ridge Model (CRM). This model ignores the tangential component of the normal vector and integrates the photometric data of v in order to determine the ridge shape at any point. Then, the two 3D surfaces

u and *v* are combined to produce the final result which is the 3D fingerprint.

The presented imaging system is simple and fast as it requires only one CCD camera, a fringe projector and a white light source for data acquisition and does not employ laser scanners or DLP projectors. Additionally, the photometric CRM algorithm takes advantage of the entire pixel resolution provided by the shading image, maximizing the resolving power of the method.

The rest of the paper is organized as follows: Section 2 describes the theoretical background and calibration processes needed for the understanding of the method. In Section 3 the experimental apparatus and the reconstruction algorithm are explained. The experimental results are presented in Section 4 and the discussion and conclusions in Sections 5 and 6 respectively.

2. Theoretical background

2.1 Reflectance model

The choice of the reflectance model depends on the properties of the examined surface, and is crucial for the success of the reconstruction. There is no universal reflectance theory to represent all known surfaces, thus each surface is described by a different reflectance equation. The Lambertian is a widely used reflectance model, adopted in many cases of diffuse surfaces. At this stage in order to use this model we will ignore subsurface scattering and specular reflection on the skin's surface due to the presence of sebum. For a scene consisting of a Lambertian surface illuminated by a single distant (parallel rays) light source, the observed surface intensity I can be simply written as the product of the composite albedo K_D, the source intensity I_0 and the cosine of the incidence angle ω_s, i.e. the angle between the direction of the incident light and the surface normal. The illumination equation involves two unit vectors, **S**, describing the light direction, and $\hat{\mathbf{n}}$ the surface normal [13]:

$$I = K_D I_0(\mathbf{S} \cdot \hat{\mathbf{n}}) = K_D I_0 \cos(\omega_s) \tag{1}$$

We assume constant albedo value on the entire finger surface. The constant albedo assumption affects only the CRM procedure, because only there the illumination equation is used. As we explain in Par. 3.5, the major albedo variations are excluded from *v*, since their frequency is smaller than the decomposition threshold.

2.2 Coordinate systems

In order to describe the properties of telecentric lenses, the equations of orthographic projection are used. In orthographic projection the magnification is independent of the object's distance from the lens, making the projection equations very simple. Their accuracy increases when the variation of the object's size along the direction of projection (conventionally the z-axis) is small compared to the mean distance between the object and the sensor [14,15]. In our experiment the height variations across the finger surface are insignificant compared to the overall distance from the camera, fact that meets the above requirements. The coordinates (x_s, y_s) of a random point at the sensor system $o_c x_s y_s$ relate to the pixel values (i,j) of the image through the following expression:

$$\begin{bmatrix} j \\ i \\ 1 \end{bmatrix} = \begin{bmatrix} \alpha & \beta & j_0 \\ 0 & \gamma & i_0 \\ 0 & 0 & 1 \end{bmatrix} \cdot \begin{bmatrix} x_s \\ y_s \\ 1 \end{bmatrix} \qquad (2)$$

where α, β, γ, i_0 and j_0 are the intrinsic parameters of the camera. The projected coordinates (x_s, y_s) connect with the camera system $o_c x_c y_c z_c$ coordinates through orthographic projection:

$$\begin{bmatrix} x_s \\ y_s \\ 1 \end{bmatrix} = \begin{bmatrix} 1 & 0 & 0 & 0 \\ 0 & 1 & 0 & 0 \\ 0 & 0 & 0 & 1 \end{bmatrix} \cdot \begin{bmatrix} x_c \\ y_c \\ z_c \\ 1 \end{bmatrix} \qquad (3)$$

The camera coordinates (x_c, y_c, z_c) are linked with the lab coordinates (X, Y, Z) of the absolute system $OXYZ$ through translation and rotation:

$$\begin{bmatrix} x_c \\ y_c \\ z_c \\ 1 \end{bmatrix} = \begin{bmatrix} r_{11} & r_{12} & r_{13} & t_x \\ r_{21} & r_{22} & r_{23} & t_y \\ r_{31} & r_{32} & r_{33} & t_z \\ 0 & 0 & 0 & 1 \end{bmatrix} \cdot \begin{bmatrix} X \\ Y \\ Z \\ 1 \end{bmatrix} \qquad (4)$$

where $R_{cw} = [r_{ij}]$ is the rotation matrix and $T_{cw} = [t_x \ t_y \ t_z]^T$ the translation vector. These two matrices define the extrinsic parameters of the system. For the sake of simplicity we choose the axes y_c-Y_w to be parallel to each other and x_c-X to lie on the X-Z plane. Additionally x_s and y_s are parallel to x_c and y_c respectively. All the above restrictions translates to $r_{12}=r_{21}=r_{23}=r_{32}=0$ and $r_{22}=1$. Given these conventions we have:

$$R_{cw} = \begin{bmatrix} \sin\theta_c & 0 & -\cos\theta_c \\ 0 & 1 & 0 \\ \cos\theta_c & 0 & \sin\theta_c \end{bmatrix} \qquad (5)$$

where θ_c is the angle formed between the X axis and the cameras optical axis z_c. The R_{cw} and T_{cw} matrices define the extrinsic parameters of the camera system. We consider only topographic surfaces represented by a height variable $f_Z(X,Y)$. Additionally we assume Lambertian reflectance, constant albedo for the surface and a distant point light source with known direction **S**. The height Z is the elevation over the X-Y plane which is marked as the reference plane P_0. At every point (X,Y) a normal vector $\hat{\mathbf{n}}(X,Y)$ is assigned:

$$\hat{\mathbf{n}} = \frac{1}{|\hat{\mathbf{n}}|} \left[\frac{\partial f_Z(X,Y)}{\partial X}, \quad \frac{\partial f_Z(X,Y)}{\partial Y}, \quad -1 \right]^T \qquad (6)$$

2.3 Camera calibration

The camera must be calibrated, both in respect of its intrinsic and extrinsic parameters. For the camera calibration the process described in [16] was followed, in which the calibrating object is an orthogonal prism containing a grid of equally spaced circular points (38×38) on the two orthogonal sides. The photogrammetric equations are solved and the camera parameters are estimated.
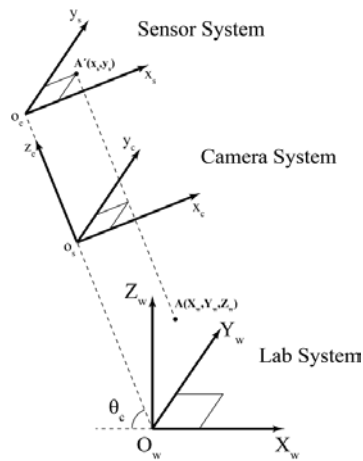
Coordinate Systems

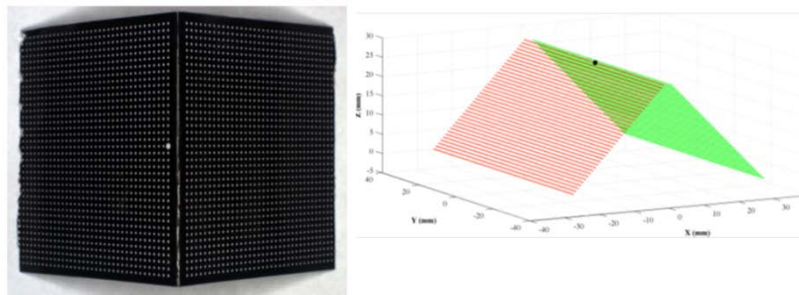**Figure 1:** The coordinate systems used.

Figure 2: Left: the camera calibration object. Right: the reconstructed white points. From Gorpas et al. [16].

2.4 Light source calibration

The CRM process requires known properties for the light source, and therefore calibration of the lighting system is needed. For that purpose we used a sphere with known radius *R* and a diffuse surface. It is known that in the case of a smooth surface the light source vector is perpendicular to the point where the illumination maximum occurs. Considering orthographic projection, on the camera coordinate system $o_c x_c y_c z_c$ the illumination maximum A has coordinates $\left(R_p \cos\varphi, R_p \sin\varphi, \sqrt{R^2 - R_p^2} \right)$, where $R_p = (O'A')$. Figure 3 shows that $\hat{\mathbf{n}} = \overrightarrow{OA'}$ and $\mathbf{S} = -\hat{\mathbf{n}}$. The lighting apparatus used has the capability of multiple light directions (Figure 5), so we chose the optimum position with the highest illumination coverage.

2.5 Fringe pattern calibration

If we assume that the fringe projection beam is perfectly collimated and with regular line spacing, it can be described by just two parameters: the angle formed between the beam vector v_p and plane P_0, and the fringe

spacing $D_{c,i}$ (Figure 6). As it is shown in Par. 3.4 only the component $\varphi_{f,x}$ of the angle projected onto the X-Z plane is required.
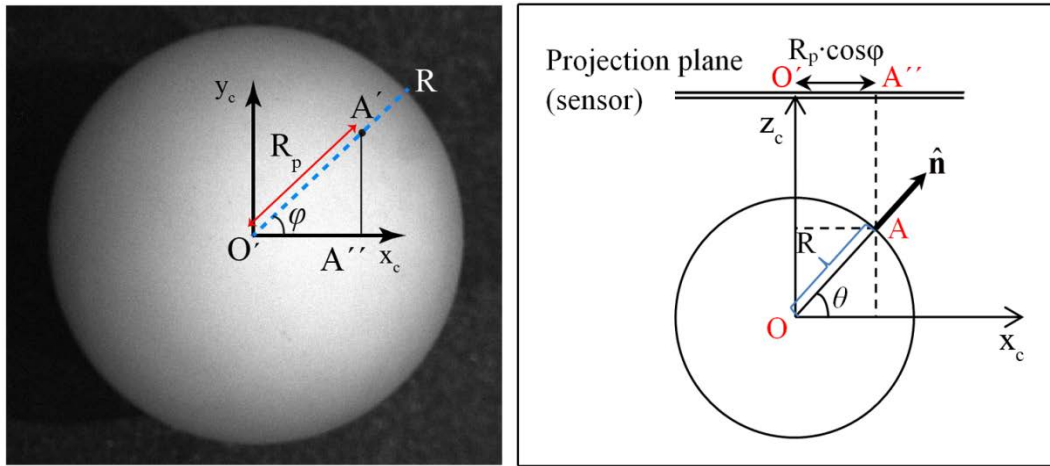

Figure 3: Light source calibration scheme.

The acquisition of these parameters is done during the fringe pattern calibration process. The angle $\varphi_{f,x}$ is estimated from the displacement of the fringes along X axis for various vertical positions of the reference plane. For that purpose we used the high accuracy Thorlabs LJ750 focusing stage with of 0.01mm precision (Figure 5d). If the increase of the vertical position of P_0 by ΔZ (where "Δ" denotes difference) leads to horizontal displacement ΔX of the fringes, then the angle $\varphi_{f,x}$ will be:

$$\varphi_{f,x} = \arctan\left(\frac{\Delta Z}{\Delta X}\right) \tag{7}$$

The quantity measured directly out of the image is the projected displacement Δx_s in the sensor system $o_s x_s y_s$, so transformation into world coordinates using Eq. 2-4 is required.

For the various vertical positions of P_0, the average spacing between the fringes is also measured, in order to test the beam's collimation. A perfectly collimated beam leaves the spacing of the projected pattern unaffected, regardless of the position of the reference plane.

The last stage of the fringe calibration is the measurement of the fringe spacing regularity. The pattern is projected on an optical flat surface and the field of view is divided into a number of segments $l_{c,i}$ parallel to the x_c axis. The spacing $D_{c,i}$ between the projected fringes is measured along $l_{c,i}$. An evenly spaced fringe pattern results to a perfect square grid of sample points, so any deviation is due to irregularities in the pattern. The fringe pattern calibration process resulted to $\varphi_{f,x} = 66,3°$, collimation error less than 1° and average deviation from square grid less that 5%.
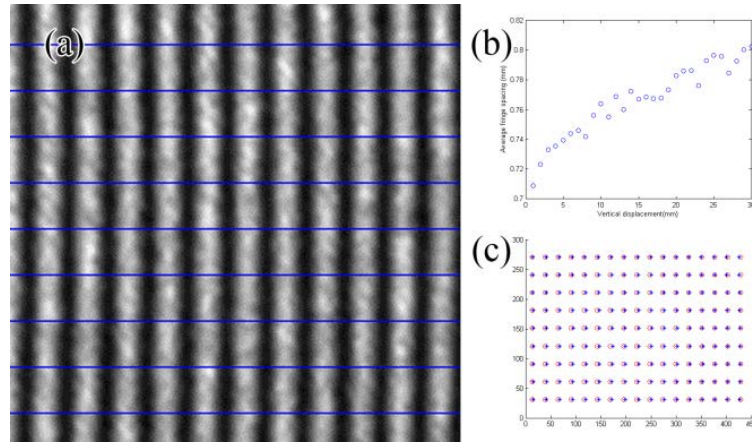
Figure 4: Fringe pattern calibration. (a) Part of the fringe pattern projected on the reference plane with sample lines $l_{c,i}$ marked with blue lines. (b) Collimation testing data. (c) Grid regularity testing.

3. Materials and Methods

3.1 Hardware Premises

The Computer Vision System used in the experiment was developed in Biomedical Optics and Applied Biophysics Laboratory in National Technical University of Athens. It includes one 1/1.8″ progressive scan digital color CCD PointGrey Scorpion SCOR-20SO camera with IEEE 1394 interface as described in [16]. The image size is 1600×1200 pixels, with pixel size of 4.4×4.4μm. A telecentric lens system is used, which is designed to minimize perspective distortion so that the equations of orthographic projection can be implemented. All telecentric lenses must be optically corrected for perspective distortion, so that objects have the same perceived size, regardless of their location in the lens field of view. Considering all these premises, the lens chosen as the most appropriate was a 0.29X Melles Griot Invarigon-R™ Telecentric Gauging Lens.

The lighting apparatus consists of an array of LED light sources, which allows us to test the method with many different lighting directions. Each LED source can be considered as a point distant ideal light source. The fringe projector consists of four parts. A blue LED source provides the illumination needed for the fringe pattern generation. A collimating lens converts the rays into a parallel beam, before passing through the fringe pattern transparency. An imaging lens projects the fringe pattern on the imaging plane. The color of the LED is blue because short wavelengths are less scattered on the skin surface in comparison to red light, making the fringes sharper.

3.2 Image acquisition process

The image acquisition process runs as follows: Two images of the finger are acquired, one with the fringe pattern projected on it and one with the fringe projector switched off. The switch between the two images is done with the camera control software Flycap2. The fringe image is reconstructed with a geometrical algorithm, as shown in Par. 3.4, resulting to the large scale component f_u of the 3D fingerprint.
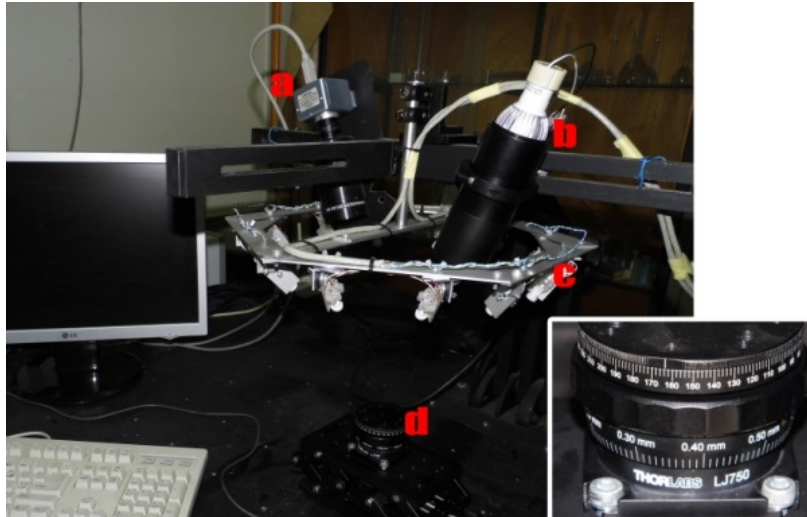
Figure 5: The experimental setup. (a) Imaging camera, (b) fringe pattern projector, (c) white light sources, (d) focusing and rotation stage.
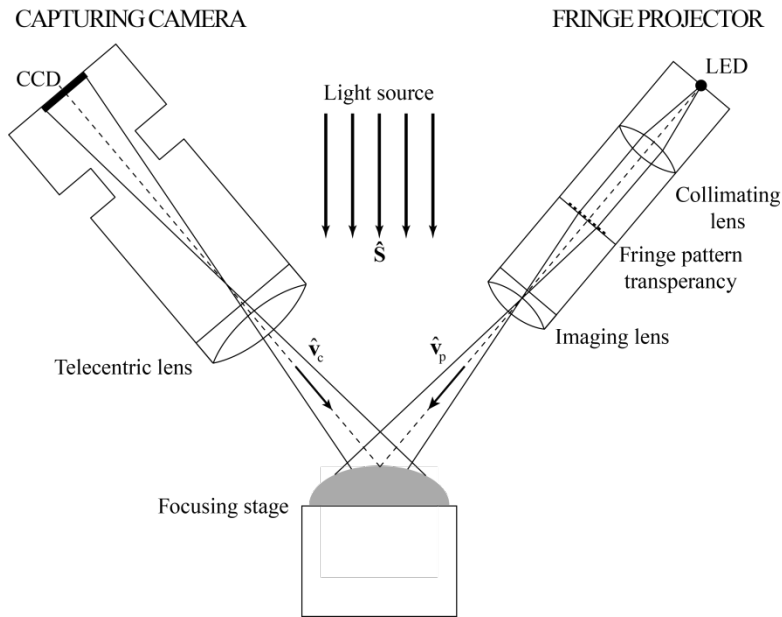

Figure 6: The experimental setup.

The shading image is decomposed into two parts with the help of an advanced Meyer algorithm. A small scale component v contains the ridge details while a large scale component u the geometric information of the finger along with the albedo changes. Small scale v is reconstructed via CRM, as shown in Par. 3.5, while u is replaced by f_u from fringe reconstruction. The image acquisition process is very fast, as it requires only two images. The computational time for the reconstruction takes a few seconds in a latest generation computer. These facts make the proposed process very fast and cost effective. Below we present a schematic description of the above process.

3.3 Image decomposition

It is widely accepted that the nature of the finger skin with its large scale (low frequency) and small scale (high frequency) features, poses many problems to reconstruction [17]. As any highly detailed surface, the finger can be regarded as a combination of a structural part, representing the large scale geometrical features, and a textural part containing the small scale finer details of the epidermal ridges. The definition of texture is quite unclear, as the threshold that separates "structure" from "texture" is subjective and depends on the nature of the surface. However, in the case of the finger the absence of most of the intermediate frequencies create a large "gap" between structural and textural components, fact that helps us separate them more easily.
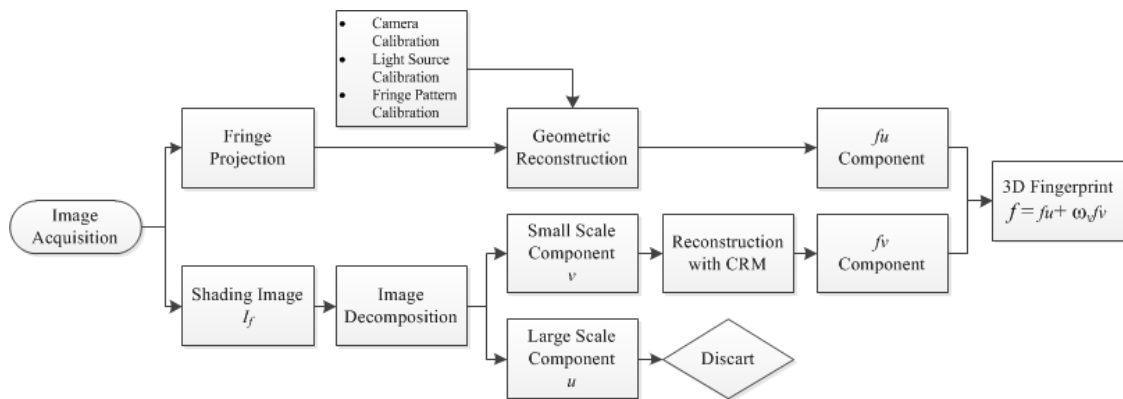

Figure 7: Schema showing the 3D fingerprint reconstruction process, form image acquisition to the extraction of the 3D fingerprint.

The solution we propose in order to deal with the complicated nature of the finger is to decompose the 2D shading image I_f into two components u and v, where u represents the large scale geometrical information of the surface (finger curvature) and v the small scale details (epidermal ridges). The scope of the image decomposition is to isolate all the high detailed features of the 2D image and reconstruct them separately, taking advantage of some special geometrical properties of the epidermal ridges in CRM. The structural part of the finger represents a rough estimation of the finger 3D surface and will be reconstructed by the fringe projection technique. For the image decomposition we use the algorithm adopted in the A^2BC model [18][19] to solve the Meyer problem [20]. The image decomposition is reduced to the following procedure consisting of two steps. Firstly with v being fixed, u comes as a solution of:

$$\inf_{u \in X} \left(J(u) + \frac{1}{2\lambda} \|f - u - v\|_X^2 \right) \tag{8}$$

and with u being fixed, v comes as a solution of:

$$\inf_{v \in G_\mu^d} \left(\|f - u - v\|_X^2 \right) \tag{9}$$

The discrete total variation J of u is defined by:

$$J(u) = \sum_{1 \leq i,j \leq N} \left| (\nabla u)_{i,j} \right| \tag{10}$$

According to [19], the iterative algorithm for the computation of *u*, *v* is:

• Initialization of *u*, *v*:

$$u_0 = v_0 = 0 \tag{11}$$

• Iterative process:

$$u_{n+1} = P_{G_\mu^d}(f - u_n) \tag{12}$$

$$u_{n+1} = f - v_{n+1} - P_{G_\lambda^d}(f - v_{n+1}) \tag{13}$$

• Iterations stop if:

$$\max \left(\left| u_{n+1} - u_n \right|, \left| v_{n+1} - v_n \right| \right) \leq \varepsilon \tag{14}$$

Chambolle in [21] suggested the following method for computing the nonlinear projection $P_{G_\lambda^d}$ iteratively:

$$p^0 = 0, \text{ and } p_{i,j}^{n+1} = \frac{p_{i,j}^n + \tau \left(\nabla \left(div\left(p^n \right) - f / \lambda \right) \right)_{i,j}}{1 + \tau \left| \left(\nabla \left(div\left(p^n \right) - f / \lambda \right) \right)_{i,j} \right|} \tag{15}$$

with $\tau \leq 1/8$. It is proven that $\lambda div(p^n)$ converges to $P_{G_\lambda^d}$ as n→∞. This algorithm needs two parameters to perform the decomposition, λ and μ. The smaller λ is, the smaller the L^2 norm of the residual *f* - *u* - *v* is, and most of the times a value of $\lambda = 1$ works fine. On the other hand, parameter μ controls the *G* norm of the oscillating component *v*, and the larger μ the more information *v* contains and *u* is more averaged. There is no universal criterion for finding the right value for the μ parameter, and mostly is done through trial and error. A proposed method for choosing the optimum value for μ is the correlation function [22-24]. In our experiments we tried 50 steps for μ determination. We concluded that $\lambda = 1.0$ and $\mu = 80$ give the optimum results (Figure 14).

3.4 Reconstruction of u with fringe projection

The reconstruction of *u* is performed by a sinusoidal fringe projection system. The fringe projector consists of a blue LED light source, a fringe pattern transparency and the collimating lens (Figure 6). A series of equally spaced straight fringes are projected on the examined surface and if the point of view deviates from the direction of the projected beam the fringes appear deformed. Given a collimated beam and a telecentric optical system, the departure of a viewed fringe from a straight line shows the departure of the examined surface from a

reference plane.

The deformed fringes are the traced and sampled along the lines $l_{c,i}$. The sampling density chosen depends on the amount of down-sampling intended for the reconstruction of *u* and is directly linked to the scale of the details planned to be restored from *v* by the CRM algorithm. The calibration process described above resulted to two vectors, $\mathbf{v}_p$ describing the direction of the fringe beam and $\mathbf{v}_c$ the camera orientation. We measure the distances $dx_{c,i}$ between the original and the deformed fringes along the segments $l_{c,i}$ in $o_c x_c y_c z_c$. The departure $\Delta h_{w,i}$ of a fringe above P_0 in OXYZ will be:

$$\Delta h_{w,i} = \frac{\sin \varphi_{f,x}}{\sin(\varphi_{f,x} + \theta_{c,x})} \cdot dx_{c,i} \qquad (16)$$

where, $\theta_{c,x}$ and $\varphi_{f,x}$ the angles formed between the reference plane P_0 and the projected on the X-Z plane components of vectors $\mathbf{v}_c$ and $\mathbf{v}_p$. This process is performed on all sample points and the 3D shape of *u*, denoted by f_u, is extracted. The points between the measurements are calculated via interpolation. This model works under the condition of a perfectly collimated fringe beam. Although perfect collimation is not feasible, the fringe testing process showed that for the height scales of the measured objects (1~2cm) the error due to poor collimation is negligible.
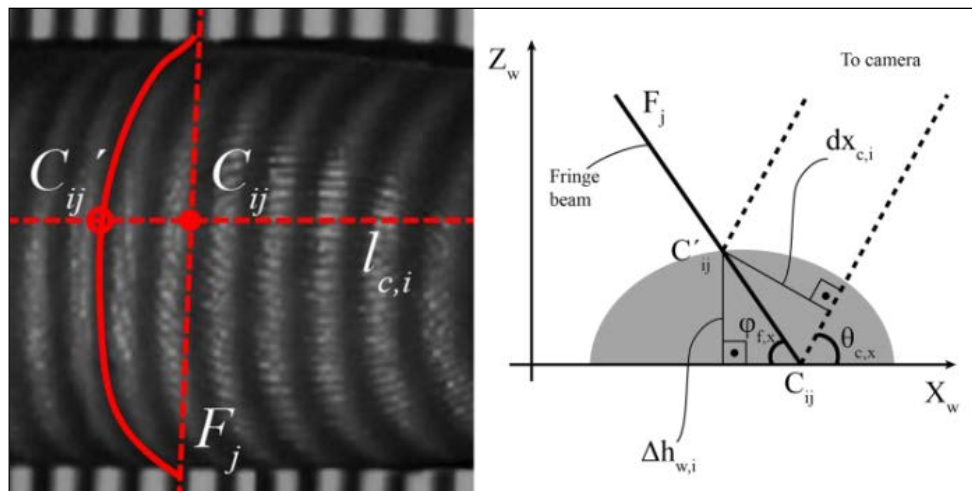

Figure 8: The fringe pattern projection. We measure the distance $dx_{c,i} = (C_{ij}C_{ij}')$ along the line $l_{c,i}$ between the reference and the deformed fringe.

3.5 Reconstruction of v with the Cylindrical Ridge Model

In CRM the integration of the illumination equation is performed along the cross-section of the ridge and since the ridges have a comparatively small cross section, the albedo change in the integration interval is considered negligible. Truly, in Figure 14 we can see that the major albedo variations are observable only in the structure component *u*, as their scale is too large to be included in *v*.

Unlike *u*, the small scale component *v* has a very complicated superficial structure, particularly difficult to

reconstruct with fringe projection, due to the technique's limited resolving power [11-12]. For the restoration of v we will use CRM, in which the epidermal ridges are considered to have a high degree of axial symmetry, resembling a system of curved semi-cylinders of almost constant height and width. The intensity gradient can be locally analyzed into two components, one tangential to the axis of cylindrical symmetry and one vertical to that axis (Figure 9). CRM relies on the assumption that on the surface of the ridges the tangential gradient component varies much slower than the transverse component, meaning that the width of the ridges changes relatively slowly. If the tangential component of the gradient is considered negligible the unknown parameters can be reduced and the reconstruction of the ridges from v is possible. We establish a local coordinate system $\tilde{o}\tilde{x}\tilde{y}\tilde{z}$ that follows the path of the ridges in 3D space, with $\tilde{x}$ and $\tilde{y}$ axes always maintaining transverse and tangent orientations respectively in relation to the ridge principle axis of symmetry at any given point. The orientation of $\tilde{z}$ axis depends on the curvature of the finger as it is always vertical to the $\tilde{x}\tilde{y}$ plane. That information is provided by f_u.

First we extract the morphological skeleton of the texture image v in order to find the thinned ridges. The skeletonization requires a binary image X_v of the ridges, which is acquired by thresholding v. The skeleton $SK(X_v)$ of the binary image X_v is the union of a series of skeleton subsets:

$$SK(X_v) = \bigcup_{r>0} \left[\left(X_v \ominus rB \right) - \left(X_v \ominus rB \right) \circ drB \right] \tag{17}$$

where rB denotes the open disk of radius r and drB is a closed disk of infinitesimally small radius dr. The small protrusions along the ridge trails are ignored. The integration of the normal vectors along a cross-section of an illuminated ridge from valley to valley can retrieve its shape. If we accept that the tangential component of the gradient is negligible in respect to the transversal, Eq. 1 can be integrated along the $\tilde{x}$ dimension. This process can be repeated along all the ridges and finally v will be reconstructed. The difficulty posed is to find the projected orientation of the $\tilde{x}$ axes on the image plane, which depending on the curvature of the finger is not always vertical to the projected SK_i trails. We map the SK_i on the reconstructed f_u surface and determine the orientation of the $\tilde{x}$ axes in XYZ space. Afterwards the $\tilde{x}$ axes are projected on the $o_s x_s y_s$ system in order to find the cross-sections $CS_i = (A_i B_i)$ along which the integration of the brightness values will be performed (Figure 10). If we assume Lambertian reflectance with almost constant albedo, the illumination intensity along the segment according to Eq. 1 ($K_D = I_0 = 1$) will be:

$$I(\tilde{x}) = \tilde{\mathbf{S}} \cdot \tilde{\mathbf{n}} = \left[\tilde{S}_x, \tilde{S}_y, \tilde{S}_z \right] \cdot \left[\tilde{n}_x, \tilde{n}_y, \tilde{n}_z \right]^T \tag{18}$$

It is important not to forget to express the $\mathbf{S}$, $\hat{\mathbf{n}}$ vectors in the $\tilde{o}\tilde{x}\tilde{y}\tilde{z}$ system. The CRM model ignores the component $\dfrac{\partial \tilde{z}}{\partial \tilde{y}}$, fact that leads to $\tilde{n}_y = 0$ and $\dfrac{\partial \tilde{z}}{\partial \tilde{x}} = \dfrac{d\tilde{z}}{d\tilde{x}}$. The height difference $\Delta \tilde{z}$ between two points A_i and B_i can be found by integrating the normal along the $\tilde{x}$ direction:

$$\Delta \tilde{z} = \int_{A_i}^{B_i} \frac{1}{\tilde{S}_x} \left(I(\tilde{x}) - \tilde{S}_z \right) d\tilde{x} \qquad (19)$$

We divide the cross-section S_i along $\tilde{x}$ axis into k discrete points with $\Delta \tilde{x}_i$ distance between them. The discrete version of Eq. 19 is used to compute the height $\tilde{z}_k$ at the kth position of the section S_i in an iterative process:

$$\tilde{z}_{k+1} = \tilde{z}_k + \frac{1}{\tilde{S}_x} \left(I_k - \tilde{S}_z \right) \Delta \tilde{x}_{k+1} \qquad (20)$$

Note that the v reconstruction process, in contrast to u, produces the relative height map of the ridges and not their absolute values, and therefore the result must be multiplied by a constant to match the ridges real depth. During the normal integration the initial height $\tilde{z}_0$ above the finger surface is always set to 0. After the integration process, the $\tilde{z}_k$ heights are converted to world coordinates. After the computation of the heights along the segment we move to the next cross-section CS_{i+1} along the ridge until the sample points are covered. After the reconstruction of v and the extraction of f_v, the final 3D model is synthesized by the two components, f_u and f_v.

3.6 Combining f_u and f_v

When u and v are reconstructed, they are combined to produce the final 3D fingerprint.

$$f_Z(\text{x,y}) = f_u(\text{x,y}) + \omega_v \cdot f_v(\text{x,y}) \qquad (21)$$

The two reconstructed surfaces f_u and f_v are combined with different weights 1 and ω_v respectively. The value of these weights depends on an estimation of the contribution that f_u and f_v have on the final surface, information that is lost during image decomposition, since the decomposed components are normalized before reconstruction. It is known that the average depth of the adult man's epidermal ridges is approximately 0.1mm [10]. The size of the reconstructed by the fringe projection process component f_u comes in real height units, since the camera and the fringe system are both calibrated. If we calculate the average ridge depth d_v of f_v, the weight ω_v will be equal to $0.1/d_v$ if f_v is measured in mm.

3.7 Digital unwrapping of the fingerprint

The 3D fingerprint introduced in this work has many advantages over the 2D one. However, it needs to be compatible with fingerprint impressions taken at crime scenes or with samples stored in fingerprint databases acquired by traditional 2D Automated Fingerprint Identification Systems (AFIS), the majority of which are touch-based devices [1]. Furthermore, all the matching methods used today in fingerprint identification, either minutiae-based or singular point-based, are based on 2D algorithms, [25]. Therefore an 'unwrapping' process needs to be integrated in our algorithm in order for it to be compatible with the current fingerprint identification and matching procedures.
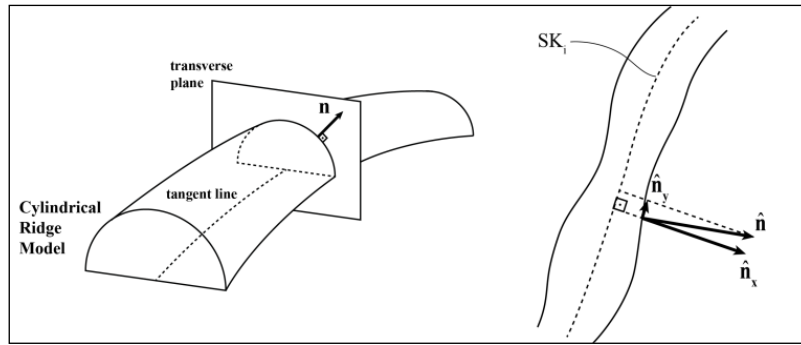
Figure 9: The Cylindrical Ridge Model geometry. Left: the ideal semi-cylindrical model. Right: CRM assumes $\hat{n}_y \approx 0$ for small tangential variations.
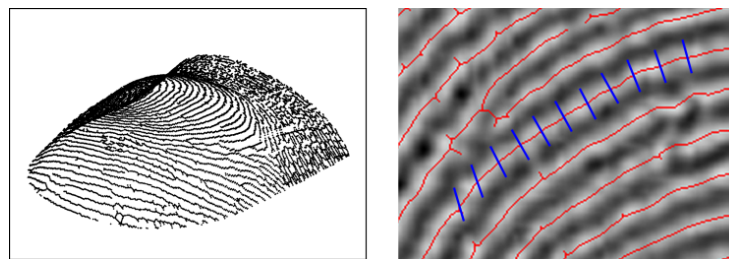

Figure 10: Left: the SK_i mapped on the finger surface provided by f_u. Right: some of the skeleton trails SK_i with corrected cross-sections (blue lines). Notice that the deviation from projected normal increases as the normal of the surface departs from the z_c axis.
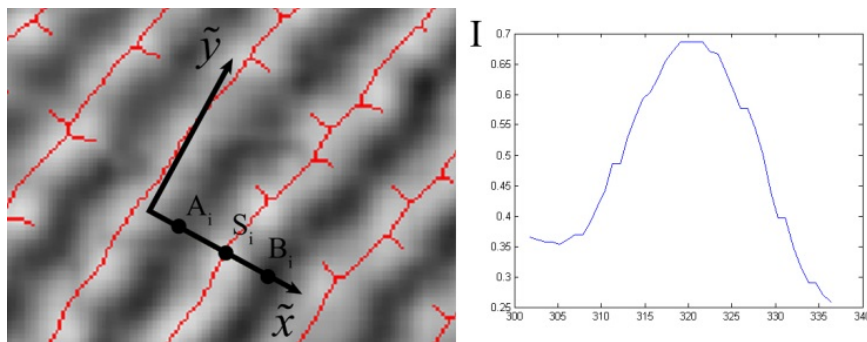

Figure 11: Left: the local system and the valley-to-valley section (A_iB_i) around sample point S_i. Right: the intensity I profile measured at (A_iB_i).

This unwrapping algorithm must take into account the flattening and rolling of the finger that occurs in standard touch-based acquisition systems. The shape of the finger affects the way the unwrapping of the fingerprint is performed, since it is not a perfect cylinder. During the orthographic projection on the CCD sensor in our system, regions of the finger with greater surface slope appear more shrunk and must be distorted proportionally in order to perform the unwrapping. Here we introduce a specialized unwrapping algorithm that takes into

account the finger curvature and its axial symmetry around the finger baseline, in order to simulate the rolling effect of the finger.

Knowing that in touch-based AFIS the finger is rolled around its principal axis (baseline), the unfolding of the 3D fingerprint will be performed in a way that preserves the geodesic distance along surface curves that lie on planes perpendicular to that baseline (Figure 12). We assume that due to the elongated nature of the finger the rolling mostly affects directions vertical to its baseline and any unwrapping in direction parallel to it will be negligible.

The type of unwrapping we will perform is called "Equidistance Unwrapping", and is a non-parametric technique that aims to preserve the geodesic distance between any two points in a local region of the finger surface. This is a desirable feature for the 3D unwrapping, as most minutiae-based matching procedures compare distances between minutiae (ridge bifurcation and ending points) for fingerprint matching and identification and any distortions could lead to matching errors.

For simplification the image is rotated so that the projected baseline is parallel to y_s axis in $o_sx_sy_s$.

A distortion map C(x,y) for all points (x,y) of the image will control the amount of stretching required in order to simulate the rolling of the fingerprint. The sampling grid consists of a number of lines l_m vertical to the baseline (thus parallel to x_s axis), divided into equal numbers of sampling points (Figure 12).

Let P'^k_m denote the *k-th* point of the *m-th* sampling line on the 2D shading image and P^k_m its corresponding on the finger surface. The numbering of the *k* index starts at the baseline and ends at the finger edge. Positive values [1 *k*] account for the right side of the finger and the negative ones [-*k* 1] for the left. The distortion factor C^k_m at *k-th* point of the *m-th* line will be:

$$C^k_m = \frac{L^k_m}{Lproj^k_m} \qquad (22)$$

where $Lproj^k_m$ is the projected distance from baseline P'^1_m to point P'^k_m along line l'_m, and L^k_m the corresponding curve length from P^1_m to P^k_m measured on the surface of the finger.

The arc length $L^{P_1P_2}$ between points P_1 and P_2 of a curve $\gamma(t) = (x(t),y(t),z(t))$ equals to the sum of all the infinitesimal arc lengths dl between these two points:

$$L^{P_1P_2} = \int_{P_1}^{P_2} \sqrt{\left(\frac{dx(t)}{dt}\right)^2 + \left(\frac{dy(t)}{dt}\right)^2 + \left(\frac{dz(t)}{dt}\right)^2}\, dt \qquad (23)$$

In its discrete form, the arc length L^k_m at sample point P^k_m along line l_m equals to the sum of all the infinitesimal arc lengths dl^i_m with $i = 1$ to k:

$$L_m^k = \sum_{i=1}^{k} dl_m^i = \sum_{i=1}^{k} \sqrt{\left(\Delta x_m^i\right)^2 + \left(\Delta z_m^i\right)^2} \qquad (24)$$

Note that the *y* dimension is absent, as the sampling lines are parallel to x_s axis. The differences $\Delta x_m^i = x_m^{i-1} - x_m^i$ and $\Delta z_m^i = z_m^{i-1} - z_m^i$ are measured at the lab coordinate system OXYZ. After the computation of the discrete distortion map, the distortion factors for all the points of the image plane are calculated via interpolation. The new 'unfolded' coordinates $\left(x_u^A, y_u^A\right)$ of point A in relation to the original ones $\left(x^A, y^A\right)$ will be:

$$\begin{aligned} x_u^A &= C(x^A, y^A) \cdot x^A \\ y_u^A &= y^A \end{aligned} \qquad (25)$$

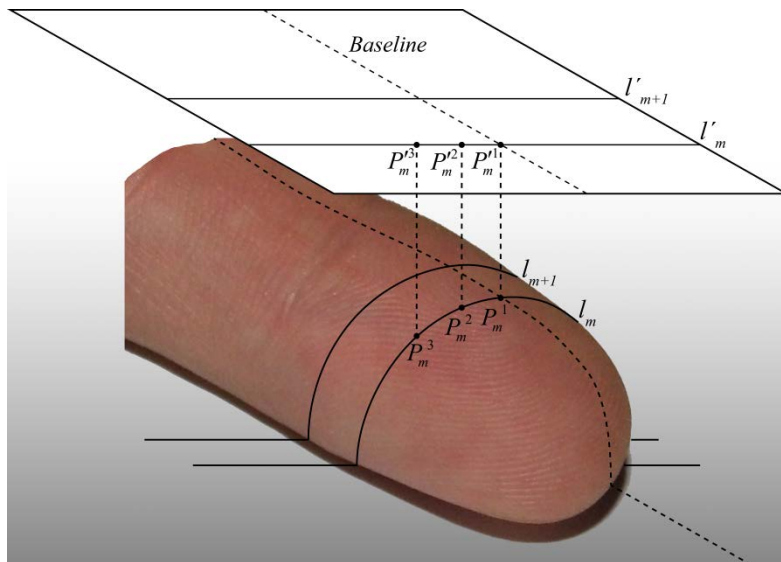The result of the application of the distortion map on the shading image is shown at Figure 13.

Figure 12: Schematic of the sample grid used for unwrapping, with orthographic projection.
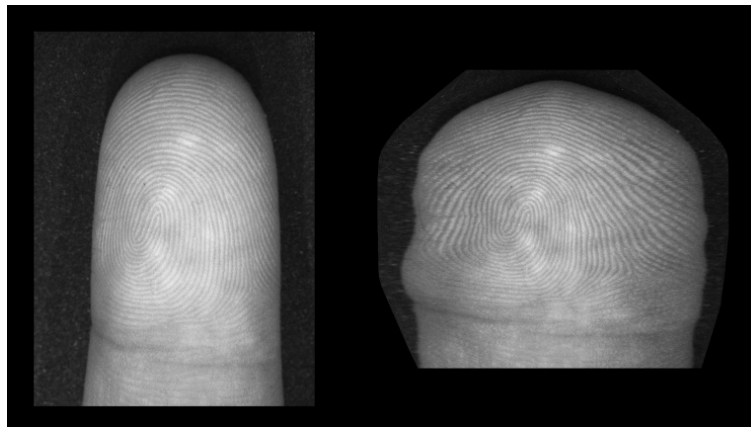

Figure 13: Left: the captured image of the finger. Right: the same image unfolded by the unwrapping algorithm.

4. Experimental Results

4.1 3D fingerprint reconstruction

The image acquisition completed in two steps. First we acquired the fringe projection image and then the shading image I_f, which was decomposed into structure u and texture v. The structural part was reconstructed via the fringe projection process, while the textural component was restored with the CRM algorithm (Figure 15). The two results were combined to produce the 3D fingerprint biometrics (Figure 16). Finally, the 3D fingerprint was unwrapped on the 2D plane using the algorithm described in Par. 3.7 to produce a traditional AFIS compatible fingerprint (Figure 13).
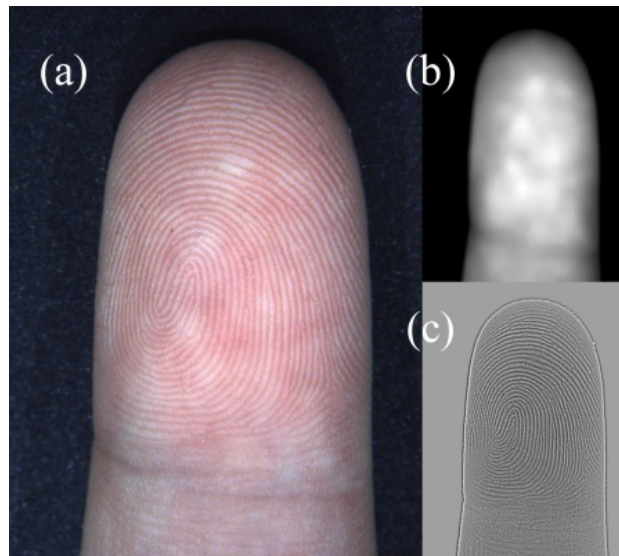

Figure 14: Image decomposition. (a) The original 2D image. (b) The structural part u. (c) The textural part v.
For the decomposition we used $\lambda = 1.0$ and $\mu = 80$.
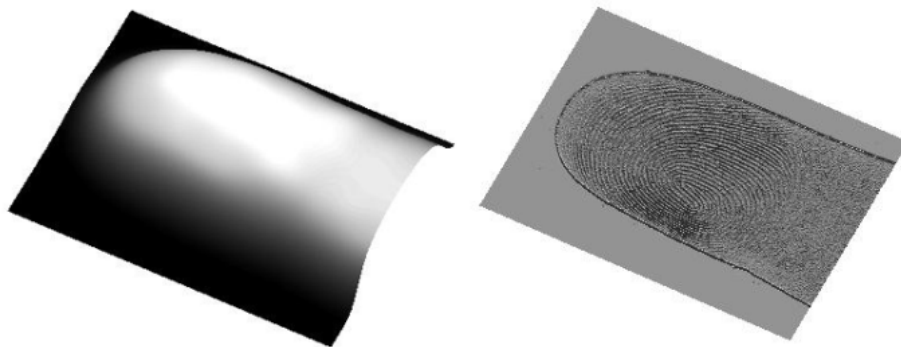

Figure 15: The reconstructed f_u (left) and f_v (right) components.

4.2 Performance evaluation

In order to evaluate the performance of our method, a reconstruction of the same finger by a reliable 3D imaging

system would be suitable for comparison. Sadly, commercial 3D non-contact systems are not common in the market, making it difficult to find one at a reasonable price to test the performance of our system.
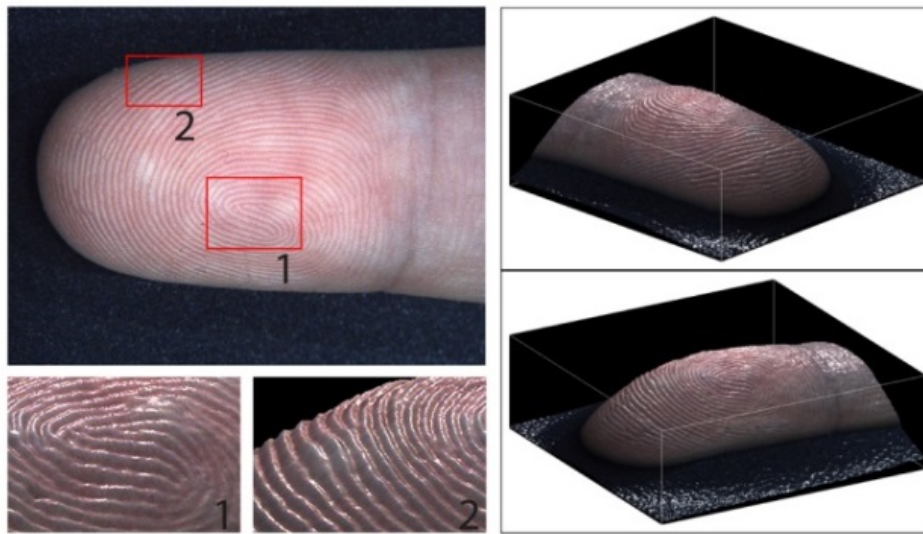

Figure 16: The 3D fingerprint with color sample by the original image and lighted.

Instead we compared the unwrapped fingerprint with ink impressions of the same finger using an advanced 2D minutiae-based matching algorithm [26]. The matching score between the two fingerprints provided a measure of the performance of our method. Unfortunately ink-based fingerprint impressions suffer from non-linear distortions due to skin deformation caused by the forced flattening of the finger. However, if we acquire a number of ink impressions, for example three, and calculate the mean position of the detected minutiae, we expect the random distortions to be averaged out.

For the extraction of the minutiae positions, a thinned image of the ridges is required. First the reconstructed ridge image f_v is thresholded by choosing a mean height as threshold, resulting to a binary image of the ridges. Afterwards this binary image is subjected to the unwrapping process described in Par. 3.7 and thinned following the procedure described in Par. 3.5. The minutiae are found by tracing along the ridges, following the technique proposed in [27].

Apart from the detection of the minutiae positions, it is essential to know the orientation of the ridges at these positions. We used a gradient-based combined method for the computation of fingerprints' orientation field proposed by Mei et al in [28]. The orientation field calculation is completed in two levels. In the first level the orientation fields with three different size blocks are calculated. These three fields are combined together to form the second level orientation field. Finally, an iteration algorithm is used to predict orientation in areas with little or no information. In order to combine the three orientation fields [28] uses a logical process: for areas with small amount of detail the large size blocks are chosen, while for highly detailed areas the small size blocks are selected. Finally, these selected local orientations are combined together to form a new orientation field, which is both robust against noise and more accurate in detailed and damaged areas than the other methods that use a single size block.

There are two main kinds of minutiae, or Galton's characteristics, considered in matching algorithms: ridge endings and ridge bifurcations. The matching algorithm we used completes in two steps. The first step is called registration, in which both fingerprints are aligned to the best degree possible. Most methods use a combination of translation, rotation and scaling for this task. After the completion of the registration process the matching of the two fingerprints follows. In the matching process a similarity score is determined by counting the corresponding minutiae pairs between the two fingerprints. Two minutiae correspond if a minutia from the test set is located within a bounding box or tolerant zone around a minutia from the template set. The matching score, which is a number in the range from 0 to 1, is calculated as the ratio of the number of matched minutiae to the total number of minutiae detected.

Before the main registration process a preliminary registration is performed by detecting and aligning the baselines (the long axis of symmetry of the finger) of the two fingerprints. Additionally the captured areas scaled to the same size. This preliminary registration aims to allow the main registration to perform with fewer errors.

Commonly a detected fingerprint minutia M_k can be described by a feature vector given by:

$$\mathbf{F}_k = (x_k, y_k, \psi_k), \tag{26}$$

where (x_k, y_k) is its coordinates on the imaging plane and ψ_k is the local ridge direction at the location of M_k. The value of ψ_k is set in the range from $-\pi/2$ to $\pi/2$, since there is no discrimination between local ridges with orientations of 90° and 270°.

Initially the image plane is sampled by three lines, with N_k sample points for each line and M_k at the center. The three lines l_1, l_2 l_3 form angles $\theta_1 = \psi_k$, $\theta_2 = \psi_k + 2\pi/3$, $\theta_3 = \theta_2 + 2\pi/3$ with the x-axis respectively. The feature vector of minutia M_k is given by:

$$\mathbf{F}_k = \left\{ \left\{ \psi_{i,lm}^k \right\}_{i=1}^{N_{lm}^k} \right\}_{m=1}^{3} \tag{27}$$

where $\psi_{i,lm}^k = d\varphi(\psi_k, \psi_{i,l_m}^k)$ is a function that calculates the difference in respect of the orientation field between the local ridge direction ψ_k of the minutia and each one of the other two sample lines l_m. The calculated feature vector is independent from any rotation or translation of the fingerprint images, and thus it can provide more reliable results for minutiae correspondences.

After the feature vectors are calculated for all minutiae, the preliminary matching for registration is performed. A similarity level between two minutiae M_i, M_j is defined as:

$$S(i, j) = \begin{cases} \dfrac{T - |\mathbf{F}_i - \mathbf{F}_j|}{T} & \text{if } |\mathbf{F}_i - \mathbf{F}_j| < T \\ 0 & \text{otherwise} \end{cases} \tag{28}$$

192

where T is a predefined threshold and $\left| F_i - F_j \right|$ is the Euclidean distance between the feature vectors $\mathbf{F}_i$ and $\mathbf{F}_j$ assigned at the two minutiae. $S(i,j) = 1$ implies a perfect match, while $S(i,j) = 0$ a certain mismatch. The values of the similarity levels help for the identification of minutiae corresponding pairs. The best matching pair is noted as the corresponding point pair and will be used in the registration process. The registration process aims to recover the geometric transformation between the test and the template fingerprint images. If the corresponding point pair is denoted by (b_1, b_2), with minutia b_1 from the input fingerprint and b_2 from the template fingerprint, the registration transformation will be:

$$\psi = D(b_2) - D(b_1) \text{ and } t = P(b_2) - R(b_1) \tag{29}$$

where R_ψ denotes the 2x2 rotation matrix of counterclockwise rotation at angle ψ and the position and ridge direction of a minutia b are denoted by $P(b) = [x(b), y(b)]^T$ and $D(b)$, respectively. Applying the estimated geometric transformation onto the test fingerprint we obtain the registered minutiae and orientation field.

Matching is performed both in respect to the position and the orientation information of the minutiae, with the use of feature vector $\mathbf{F}_k$. The position-based matching score will be:

$$M_m = \frac{\sum_{i,j} S(i,j)}{\max\{N_1, N_2\}} \tag{30}$$

where $S(i,j)$ is the similarity level of the (i,j) corresponding minutiae pair computed according to Eq. (28) and N_1, N_2 the number of minutiae detected in the common area of the test and template fingerprints, respectively. For the orientation matching the fingerprint images are divided in a number of blocks. The orientation field matching score M_o is defined by:

$$M_o = \frac{\sum_{B_i, B_j} S(B_i, B_j)}{N} \tag{31}$$

where (B_i, B_j) is the corresponding orientation block pair of the test and template fingerprint respectively, N is the number of overlapped blocks of both fingerprints, and $S(B_i, B_j)$ is the orientation similarity level calculated by Eq. (28). The final matching score M_s is computed as follows:

$$M_s = \omega_m M_m + \omega_o M_o \tag{32}$$

where (ω_m, ω_o) are weights associated with the minutia matching score M_m and the orientation field matching score M_o.

The performance evaluation experiment showed a matching score of 85%, which is considered to be very satisfying.

Note: As we can clearly see in Figure 17 the ridges at the border area of the fingerprint are distorted

disproportionally, mainly due to the fact that the surface slope is so great that pushes the orthographic condition assumed for the lens to its limits. It is known that in extreme surface slope angles all telecentric lenses deviate from ideal conditions, but in our case the distortion happens only to 5% or less of the captured area, which can be excluded from the experiments without significant loss.
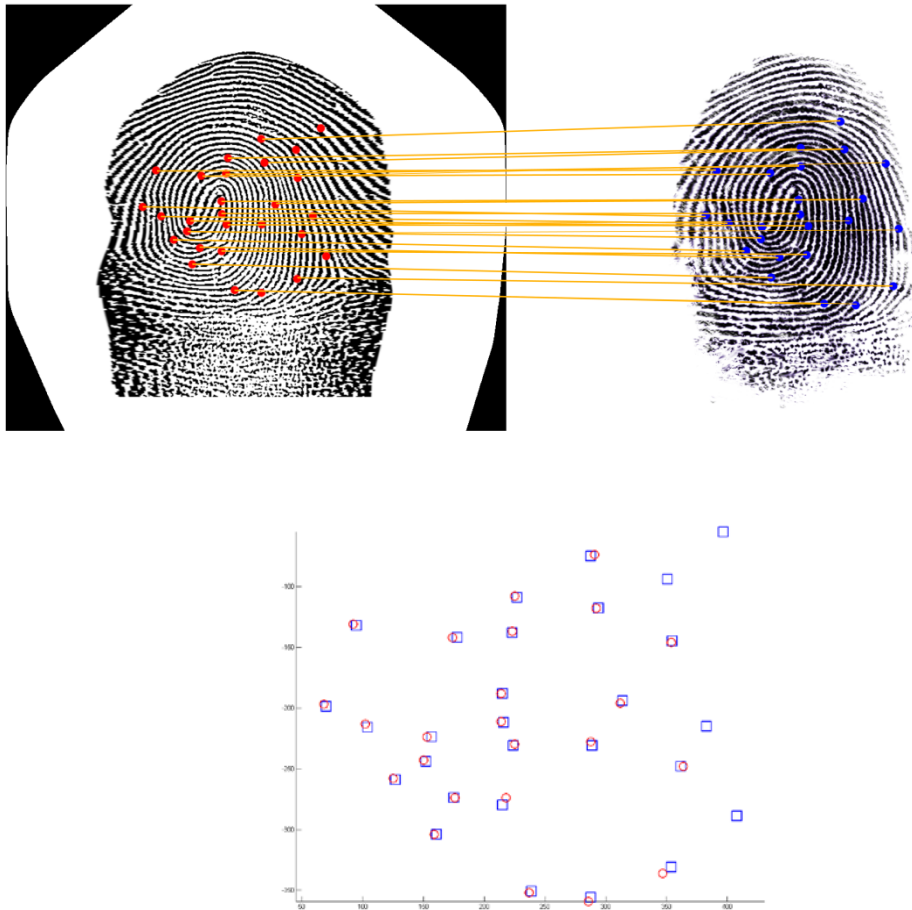

Figure 17: The corresponding minutiae pairs superimposed over the unfolded digital fingerprint (top-left) and the one of the ink impressions (top-right). At the bottom figure we can see the paired minutiae along with some that ended without a pair during the matching process.

5. Discussion

We proposed a touch-less, single-view 3D fingerprint acquisition method for 3D fingerprint reconstruction. This new method adds the third dimension (height) as an additional parameter for fingerprint coding. The detected minutiae can be assigned with two new features: the z-position and the z-component the orientation vector. These new features are able to increase the performance of the identification process and the new 3D fingerprint database has the potential of replacing the traditional 2D databases.

Minutiae of this 3D fingerprint will be described by a new feature descriptor $F = \{\mathbf{r}, \mathbf{\psi}\}$ that includes these new

parameters, where $\mathbf{r} = [x, y, z]^T$ and $\boldsymbol{\psi} = [\psi_x, \psi_y, \psi_z]^T$ denote the vectors describing the position and orientation of the minutiae in space respectively. The orientation vector $\boldsymbol{\psi}$ is computed by finding the tangent of the ridge curves in three dimensions.

The main advantage of our method compared to traditional 2D techniques, besides the additional spatial dimension, is its non-contact nature, which makes it independent from nonlinear distortions due to skin flattening. The area of interest of the unfolded fingerprint has approximately the same size with the traditional ink impression, but it excels in clearness and is distortion free.

Another main advantage of the experimental apparatus is its simplicity and low cost, as it includes a single camera, a simple lighting apparatus and a fringe projection system. The single camera feature does not require multi view stereo-calibration and the image combining algorithms, which are very complicated procedures and often introduce errors.

In order to deal with the reduced resolving power of the fringe method, an innovative feature was proposed: the decomposition of the 2D shading image I_f into two components, u containing geometrical information of the finger and v containing textural information. In this way we managed to isolate the high details of the finger that correspond to the epidermal ridges. The u component was reconstructed with the standard fringe technique, while the v component with the Cylindrical Ridge Model (CRM) algorithm. Our method takes advantage of the simplicity of the fringe technique, while exploiting the entire pixel resolution of the image with CRM, which is a photometric algorithm.

The experimental technique proposed is a prototype and we plan to examine some important issues in order to improve it. Future work will include the generalization of the skin reflectance model towards more realistic skin conditions. This new model will take into account the propagation of light through the epidermis and the subsurface scattering that occurs [29,30]. Studies with multilayer models that include backscattering, [31-32], are being considered. Furthermore, our intentions are to integrate an albedo calculating algorithm like [33-35] into our method, in order to correct albedo micro-variations on the human skin. Another step towards the upgrading of our technique is the adjustment of the illumination equations so that non-ideal light sources can be used. Finally, a pressure distortion model like [36] is planned to be integrated into the unwrapping algorithm, in order to simulate the elastic deformations of the skin during the rolling procedure.

6. Conclusions

In this paper we presented a complete non-contact, single-camera imaging system for 3D fingerprint reconstruction. This system implements an advanced hardware apparatus with telecentric vision, fringe pattern projection and photometric reconstruction. The single-view feature makes the system simple while its non-contact nature prevents errors due to skin distortion caused by forced flattening of the finger.

The reconstruction method we propose includes two innovative features: the image decomposition feature and the implementation of a new photometric reconstruction technique referred to as the Cylindrical Ridge Model or CRM.

Image decomposition separates structure from texture with the implementation of an advanced Meyer algorithm, in order to reconstruct the two modules separately. The structural part of the shading image is reconstructed with a fringe projection technique, while the textural component is restored by CRM. CRM takes advantage of the symmetrical nature of the ridges in order to treat them as a semi-cylindrical structure. The reconstructed texture is then combined with the structural to produce the final 3D fingerprint.

In order for the 3D fingerprint to be compatible with legacy rolled images acquired by traditional AFIS, an advanced unwrapping algorithm was implemented to digitally unfold the 3D fingerprints on a 2D surface. The performance of our method was evaluated by a matching experiment between the unfolded reconstructed fingerprint and an ink impression of the same finger. The results were very satisfying.

Conclusively, the proposed system provides a promising standard for 3D non-contact fingerprint acquisition ad reconstruction with the advantages of being simple, low-cost, and reliable.

References

[1]. J.A.Unar et al. "A review of biometric technology along with trends and prospects". Pattern Recognition, vol. 47, pp. 2673–2688, 2014.

[2]. F. Liu, D. Zhang. "3D fingerprint reconstruction system using feature correspondences and prior estimated finger model". Pattern Recognition. vol. 47, pp. 178-193, 2013.

[3]. S. Huang et al. "3D fingerprint imaging system based on full-field fringe projection profilometry". Optics and Lasers in Engineering, vol. 52, pp 123-130, 2013.

[4]. Qijun Zhao et al. "3D to 2D fingerprints: Unrolling and distortion correction", in Proceedings of Biometrics (IJCB)-International Joint Conference on Biometrics Compendium, IEEE, 2011.

[5]. R. Hartley. Multiple view geometry in computer vision. Cambridge, U.K: Cambridge University Press, 2000.

[6]. C. Hernandez et al. "Multi-view photometric stereo", in IEEE T. Pattern Anal, vol. 30, 2008, pp. 548–554.

[7]. F. Blais et al. "Practical considerations for a design of a high precision 3D laser scanner system". Proceedings of SPIE 959, 1988, pp. 225–246.

[8]. B. Bradley et al. "A simple, low cost, 3D scanning system using the laser light-sectioning method", in Proceedings of the IEEE International Instrumentation and Measurement Technology Conference, Victoria, Vancouver Island, Canada, May2002, pp. 299–304.

[9]. G. Hu, G. Stockman. "3D surface solution using structured light and constraint propagation". IEEE Transactions on Pattern Analysis and Machine Intelligence, vol. 11, pp. 390–402, 1989.

[10]. M. Kucken, A. C. Newell. "Fingerprint formation". Journal of Theoretical Biology, vol. 235, pp. 71–83, 2005.

[11]. Lee O et al. "An optimized in vivo multiple-baseline stereo imaging system for skin wrinkles". Optics Communications, vol. 283, pp. 4840–4845, 2010.

[12]. J. Huang, Q. Wu. "A new reconstruction method based on fringe projection of three-dimensional measuring system". Optics and Lasers in Engineering, vol. 52, pp. 115-122, 2013.

[13]. M. Oren, S. K. Nayar. "Generalization of the Lambertian Model and Implications for Machine Vision". International Journal of Computer Vision, vol. 14, pp. 227-251, 1995.

[14]. O. Faugeras. Three-dimensional Computer Vision: A Geometric Viewpoint. Cambridge Massachusetts, USA: MIT Press, 2001.

[15]. B. K. P. Horn. Robot vision. Cambridge Massachusetts, USA: MIT Electrical Engineering and Computer Science, MIT Press, 1986.

[16]. D. Gorpas, K. Politopoulos, D. Yova. "A binocular machine vision system for three-dimensional surface measurement of small objects". Computerized Medical Imaging and Graphics, vol 31, pp. 625-637, 2007.

[17]. Soweon Yoon. "Fingerprint recognition: models and applications". PhD Thesis, Michigan State University, USA, 2014.

[18]. J.-F. Aujol et al. "Image decomposition into a bounded variation component and an oscillating component". Journal of Mathematical Imaging and Vision, vol. 22, pp. 71–88, 2005.

[19]. J.-F. Aujol et al. "Image decomposition application to SAR images". Lecture Notes in Computer Science, vol. 2695, pp. 297-312, 2003.

[20]. Y. Meyer. The Fifteenth Dean Jacqueline B. Lewis Memorial Lectures, Topic: "Oscillating patterns in image processing and in some nonlinear evolution equations". American Mathematical Society Boston, MA, USA, 2001.

[21]. A. Chambolle. "An algorithm for total variation minimization and applications". Journal of Mathematical Imaging and Vision, vol. 20, pp. 89–97, 2004.

[22]. J.-F. Aujol et al. "Structure-texture image decomposition - modeling, algorithms, and parameter selection". International Journal of Computer Vision, vol. 67, pp. 11-136, 2005.

[23]. L. Rudin et al. "Nonlinear total variation based noise removal algorithms". Physica D, vol. 60, pp. 259-268, 1992.

[24]. L. A. Vese, S. J. Osher. "Modeling textures with total variation minimization and oscillating patterns in image processing". Journal of Scientific Computing, vol. 19, pp. 553-572, 2002.

[25]. Y. Chen et al. "3D touchless fingerprints: compatibility with legacy rolled images" in Proccedings of Biometric Consortium Conference, Baltimore, Aug. 2006, pp. 1-6.

[26]. Jin Qi, Y. Wang. "A robust fingerprint matching method". Pattern Recognition, vol. 38, pp. 1665-1671, 2005.

[27]. J. Feng. "Combining minutiae descriptors for fingerprint matching". Pattern Recognition, vol. 41, pp. 342-352, 2008.

[28]. Y. Mei et al. "A gradient-based combined method for the computation of fingerprints' orientation field". Image and Vision Computing, vol. 27, pp. 1169-1177, 2009.

[29]. T. Lister et al. "Optical properties of human skin". Journal of Biomedical Optics, vol. 17, 2012.

[30]. A. N. Bashkatov et al. "Optical properties of skin subcutaneous, and muscle tissues: a review". Journal of Innovative Optical Health Sciences, vol. 4, pp. 9-38, 2011.

[31]. R. Ohtsuki et al. "Multiple-reflection model lof human skin and estimation of pigment concentrations". Optical Review, vol. 19, pp. 254–263, 2012.

[32]. L. Li, C. So-ling Ng. "Rendering human skin using a multi-layer reflection model". International

Journal of Mathematics, vol. 3, pp. 44-53, 2009.

[33]. S. Biswas et al. "Robust estimation of albedo for illumination-invariant matching and shape recovery". IEEE Transactions on Pattern Analysis & Machine Intelligence. vol. 31, pp. 884-899, 2008.

[34]. J. T. Barron, J. Malik. "Shape, albedo, and illumination from a single image of an unknown object" in Proceedings of Computer Vision and Pattern Recognition (CVPR), 2012, pp. 334-341.

[35]. S. Suh, M. Lee. "Robust albedo estimation from a facial image with cast shadow under general unknown lighting". IEEE T. Image Processing, vol. 22, pp. 391-401, 2012.

[36]. D. Maltoni, R. Cappelli. "Advances in fingerprint modeling". Image and Vision Computing, vol 27, pp. 258-268, 2009.